The Astrophysical Journal Letters, 879:L4 (7pp), 2019 July 1 https://doi.org/10.3847/2041-8213/ab2768

Hard-state Accretion Disk Winds from Black Holes: The Revealing Case of MAXI J1820+070

T. Muñoz-Darias[1,2], F. Jiménez-Ibarra[1,2], G. Panizo-Espinar[1,2], J. Casares[1,2], D. Mata Sánchez[3], G. Ponti[4,5], R. P. Fender[6], D. A. H. Buckley[7], P. Garnavich[8], M. A. P. Torres[1,2,9], M. Armas Padilla[1,2], P. A. Charles[10], J. M. Corral-Santana[11], J. J. E. Kajava[12], E. J. Kotze[7,13], C. Littlefield[8], J. Sánchez-Sierras[2], D. Steeghs[14], and J. Thomas[7]

[1] Instituto de Astrofísica de Canarias, E-38205 La Laguna, Tenerife, Spain; teo.munoz-darias@iac.es
[2] Departamento de Astrofísica, Universidad de La Laguna, E-38206 La Laguna, Tenerife, Spain
[3] Jodrell Bank Centre for Astrophysics, The University of Manchester, Manchester M13 9PL, UK
[4] Istituto Nazionale di Astrofisica, Osservatorio Astronomico di Brera, Via E. Bianchi 46, I-23807 Merate, Italy
[5] Max Planck Institute fur Extraterrestriche Physik, D-85748 Garching, Germany
[6] Department of Physics, Astrophysics, University of Oxford, Keble Road, Oxford OX1 3RH, UK
[7] South African Astronomical Observatory, PO Box 9, Observatory 7932, Cape Town, South Africa
[8] Department of Physics, University of Notre Dame, Notre Dame, IN 46556, USA
[9] SRON, Netherlands Institute for Space Research, Sorbonnelaan 2, NL-3584 CA Utrecht, The Netherlands
[10] Department of Physics and Astronomy, University of Southampton, Highfield, Southampton SO17 1BJ, UK
[11] European Southern Observatory (ESO), Alonso de Córdova 3107, Vitacura, Casilla 19, Santiago, Chile
[12] Finnish Centre for Astronomy with ESO (FINCA), FI-20014 University of Turku, Finland
[13] Southern African Large Telescope, P.O. Box 9, Observatory, 7935, South Africa
[14] Department of Physics, University of Warwick, Gibbet Hill Road, Coventry CV4 7AL, UK
Received 2019 May 18; revised 2019 June 6; accepted 2019 June 6; published 2019 June 28

Abstract

We report on a detailed optical spectroscopic follow-up of the black hole (BH) transient MAXI J1820+070 (ASASSN-18ey). The observations cover the main part of the X-ray binary outburst, when the source alternated between hard and soft states following the classical pattern widely seen in other systems. We focus the analysis on the He I emission lines at 5876 and 6678 Å, as well as on Hα. We detect clear accretion disk wind features (P-Cyg profiles and broad emission line wings) in the hard state, both during outburst rise and decay. These are not witnessed during the several months long soft state. However, our data suggest that the visibility of the outflow might be significantly affected by the ionization state of the accretion disk. The terminal velocity of the wind is above $\sim$1200 km s^{-1}, which is similar to outflow velocities derived from (hard-state) optical winds and (soft-state) X-ray winds in other systems. The wind signatures, in particular the P-Cyg profiles, are very shallow, and their detection has only been possible thanks to a combination of source brightness and intense monitoring at very high signal-to-noise. This study indicates that cold, optical winds are most likely a common feature of BH accretion, and therefore, that wind-like outflows are a general mechanism of mass and angular momentum removal operating throughout the entire X-ray binary outburst.

Key words: accretion, accretion disks – stars: black holes – stars: winds, outflows – X-rays: binaries

1. Introduction

Disk winds are observed in accreting black holes (BHs) across the full range of masses (Fabian 2012; Díaz Trigo & Boirin 2016; Ponti et al. 2016). In stellar-mass BHs, X-ray winds have been established as a fundamental property of their most radiatively efficient outburst phases, the so-called soft states, likely impacting on the accretion process. However, these highly ionized (hot) winds are scarcely observed during the typically dimmer hard states, where most of the BHs of the universe exist and kinetic feedback from jets dominates (Miller et al. 2006; Neilsen & Lee 2009; Neilsen et al. 2011; Ponti et al. 2012; Fender & Muñoz-Darias 2016). The disappearance of the wind in the hard state is a matter of strong debate and has been suggested to be related to different physical processes, such as the details of the wind-launching mechanism, photoionization instabilities and over-ionization of the ejecta (e.g., Chakravorty et al. 2013; Bianchi et al. 2017; Gatuzz et al. 2019). In addition, the presence of a continuous, state-independent wind has been proposed as a viable mechanism to explain the high efficiency of angular momentum removal inferred from fits to X-ray light curves (Tetarenko et al. 2018). Low-ionization (cold) disk winds, on the other hand, have been detected via optical/infrared observations in the luminous and violent outbursts of V404 Cyg (Muñoz-Darias et al. 2016 (hereafter MD16), Muñoz-Darias et al. 2017; Rahoui et al. 2017; Mata Sánchez et al. 2018; see also Casares et al. 1991) and V4641 Sgr (Chaty et al. 2003; Lindstrøm et al. 2005; Muñoz-Darias et al. 2018). These are also thought to severely impact on accretion properties, with mass outflow rates significantly exceeding the accretion rate (MD16, Casares et al. 2019).

MAXI J1820+070 (hereafter J1820+070) was initially discovered as an optical transient by the All-Sky Automated Survey for Supernovae (and named ASASSN-18ey; Tucker et al. 2018) and then as an X-ray transient by the Monitor of All-sky X-ray Image (MAXI; Matsuoka et al. 2009). It was classified as a BH candidate based on its multi-wavelength properties (Baglio et al. 2018; Bright et al. 2018; Kawamuro et al. 2018; Kennea et al. 2018; Shidatsu et al. 2018; Tucker et al. 2018). The system is among the brightest BH transients ever observed (Corral-Santana et al. 2016), with an X-ray flux of $\sim$4 Crab and an optical magnitude of $g \sim 11.2$ at outburst peak (Shidatsu et al. 2019). In this Letter, we report on an intensive optical spectroscopic follow-up campaign obtained

Table 1
Observing log, X-Ray State, and Emission Line Properties

Epoch	Date (hh:mm)	Tel.	State[a]	He I[b]	Hα[b]
1	15/03 (14:46)	Keck	Hard	–	P-Cyg(*)
2	16/03 (08:03)	Very Large Telescope (VLT)	Hard	P-Cyg	P-Cyg(*)
3	17/03 (05:26)	Gran Telescopio Canarias (GTC)	Hard	P-Cyg	P-Cyg(*)
4	18/03 (06:09)	GTC	Hard	BW	BW
5	20/03 (05:58)	GTC	Hard	BW	BW
6	20/03 (08:07)	VLT	Hard	BW	BW
7	21/03 (06:11)	GTC	Hard	P-Cyg	BW+P-Cyg
8	22/03 (05:38)	GTC	Hard		BW
9	22/03 (07:53)	VLT	Hard		BW
10	24/03 (05:38)	GTC	Hard		BW
11	26/03 (04:29)	GTC	Hard	P-Cyg	BW
12	23/04 (02:26)	South African Large Telescope (SALT)	Hard	P-Cyg(*)	BW+P-Cyg
13	13/05 (02:03)	SALT	Hard		
14	14/05 (01:04)	SALT	Hard		
15	17/05 (00:53)	SALT	Hard		
16	17/06 (21:26)	Telescopio Nazionale Galileo (TNG)	Hard	–	
17	18/06 (04:55)	TNG	Hard	–	
18	18/06 (21:59)	TNG	Hard	–	
19	08/07 (02:05)	GTC	Soft	?	
20	10/07 (21:33)	GTC	Soft		
21	11/07 (21:26)	GTC	Soft		
22	13/07 (01:29)	VLT	Soft		
23	15/07 (01:28)	GTC	Soft		
24	18/07 (01:42)	GTC	Soft		
25	18/07 (21:42)	GTC	Soft		
26	24/07 (22:49)	GTC	Soft		
27	27/07 (21:29)	GTC	Soft		
28	03/08 (23:20)	GTC	Soft		
29	09/08 (22:18)	GTC	Soft		
30	15/08 (21:41)	GTC	Soft		
31	19/08 (21:56)	GTC	Soft		
32	07/09 (00:58)	VLT	Soft		
33	28/09 (23:57)	VLT	Hard	P-Cyg	BW
34	29/09 (23:51)	VLT	Hard	P-Cyg	
35	12/10 (21:35)	GTC	Hard		
36	21/10 (21:19)	GTC	Hard		
37	04/11 (19:45)	GTC	Hard		

Notes.
[a] X-ray state based on MAXI data.
[b] Detection of P-Cyg profiles and broad emission line wings (BWs). See the text for those marked (*). The hyphen (–) indicates lack of spectral coverage.

with a suite of the largest telescopes providing high signal-to-noise data.

2. Observations

We carried out spectroscopy during 37 epochs, which cover in great detail the different phases of the outburst (see Table 1).

2.1. Gran Telescopio Canarias (GTC)

We observed the target with OSIRIS (Cepa et al. 2000) attached to the GTC, at the Observatorio del Roque de los Muchachos (ORM) in La Palma, Spain. We used grisms R2500R (5575–7685 Å) and R2500V (4500–6000 Å), which combined with a 1.0 arcsec slit provide a velocity resolution of $\sim$200 km s^{-1}. In total we obtained 93 spectra across 22 different nights with on-source times in the range of 300–840 s.

2.2. Very Large Telescope (VLT)

J1820+070 was observed in seven different epochs with the X-shooter spectrograph (Vernet et al. 2011) attached to the VLT-UT2 at Cerro Paranal, Chile. The instrument has three different arms covering the ultraviolet, visible, and near-infrared spectral ranges, but only the first two were included in this study (the full spectroscopic database will be presented in a forthcoming work). For each epoch, we obtained 8 to 16 exposures with total on-source time in the range of 1560–2256 s. We used slit-widths of 0.9 and 1.0 arcsec in the visible and ultraviolet arms, which rendered a velocity resolution of $\sim$35 km s^{-1}.

2.3. The Southern African Large Telescope (SALT)

Spectroscopy was obtained on four separate nights with SALT (Buckley et al. 2006) situated at the South African Astronomical Observatory in Sutherland, using the Robert

Stobie Spectrograph (Burgh et al. 2003). We used the PG1300 grating and a 1.5 arcsec slit-width, which gave a wavelength coverage of 4580−6630 Å at a mean velocity resolution of ∼200 km s^{-1}. Sets of continuous 25 s exposures were obtained and combined (on-source time between 1950 and 2450 s).

2.4. Telescopio Nazionale Galileo (TNG)

We observed the target with the TNG during three epochs over two consecutive nights. Observations were taken with the spectrograph DOLORES. We used a slit-width of 1.0 arcsec together with grisms V486 (4612–4838 Å; 400 s on-source) and VHR-R (6238–7717 Å; 300 s on-source), which resulted in velocity resolutions of 50 and 120 km s^{-1}, respectively.

2.5. Keck Observatory

Our first observing epoch was taken with the Low Resolution Imaging Spectrometer (LRIS; Oke et al. 1995) attached to the Keck I telescope on Maunakea (Hawaii, USA). The red and blue arms of the spectrograph were divided using the 560 nm dichroic. On the blue side we employed the 600/4000 grism (3040–5630 Å), while on the red arm we used the 900/5500 grating (6034–8440 Å). The 0.7 arcsec wide slit provided a velocity resolution in the range of 100–180 km s^{-1}. A total of 12 × 15 s spectra were obtained in the red and 16 × 15 s spectra in the blue.

3. Analysis and Results

The long-slit spectra were reduced, extracted, and wavelength- and flux-calibrated using standard IRAF tools or the PySALT package (Crawford et al. 2016) tailored for SALT data. The X-shooter spectra were processed and combined using version 3.2.0 of the EsoReflex pipeline. We used MOLLY and custom software under PYTHON to perform the analysis. In order to increase the signal-to-noise ratio we henceforth focus on average spectra computed for each observing epoch (Table 1).

As previously reported by Tucker et al. (2018), the spectra are very rich in emission lines, including the Balmer series as well as several He I and He II transitions. Our multi-epoch observations show that their shape and strength change dramatically throughout the outburst. We observe strong line asymmetries, especially during the early stages of the outburst, as well as shallow P-Cyg profiles and broad, non-Gaussian emission line wings. These features are standard accretion disk wind signatures, similar to those observed in V404 Cyg (MD16) and V4641 Sgr (Muñoz-Darias et al. 2018). Figures 1 and 2 show a suite of the different emission line behaviors present in our data, albeit we do not show every spectrum for clarity reasons (however, see Table 1 for a full summary). In particular, P-Cyg profiles are best detected in He I 5876 Å (He I–5876 hereafter), while asymmetries and broad emission wings are best seen in Hα, which is the strongest optical emission line. We note that these are also typical outflow tracers in other stellar classes. In particular, He I–5876 is one of the best optical wind markers in massive stars, and P-Cyg profiles in this line together with broad Hα wings are a common feature in O supergiants (e.g., Prinja & Fullerton 1994). Likewise, disk-dominated accreting white dwarfs can show, in addition to P-Cyg profiles in ultraviolet resonance lines, wind signatures in He I–5876 and Hα (Kafka & Honeycutt 2004).

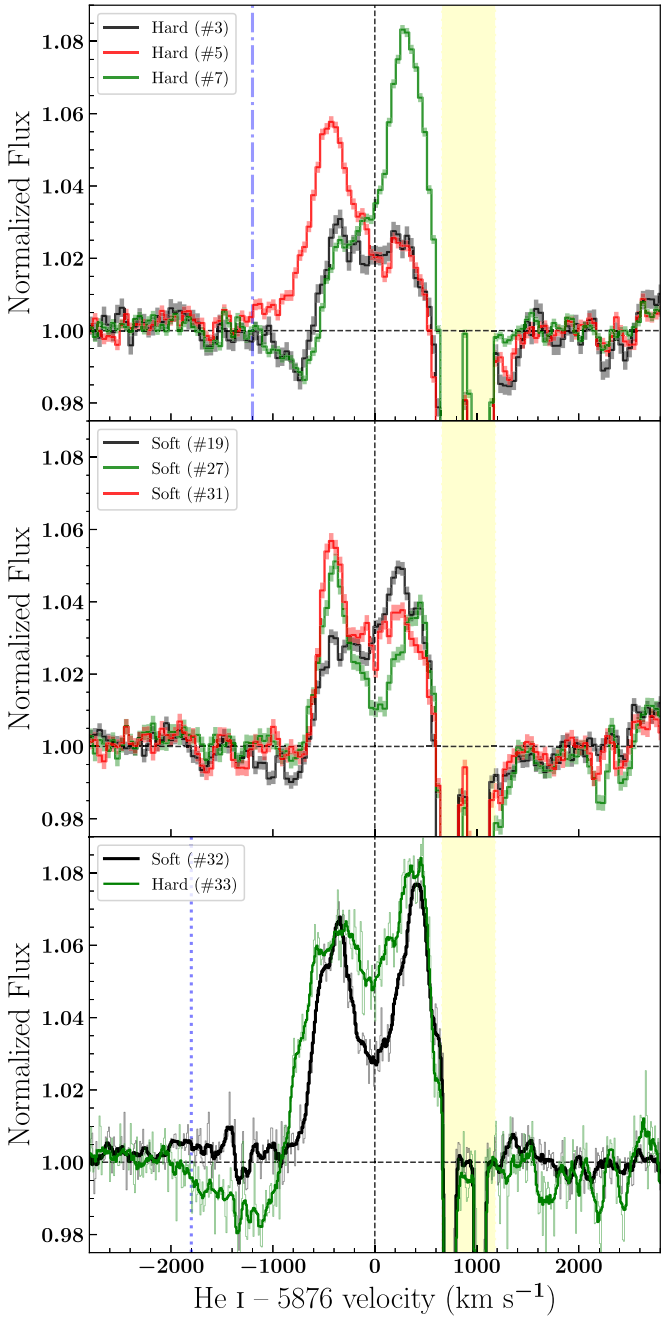

Figure 1. Evolution of He I–5876. Top panel: example of hard-state wind features detected during outburst rise. P-Cyg profiles show the presence of a wind with $V_t \sim 1200$ km s^{-1} (dashed–dotted line). One epoch showing a broad (blue) wing is also represented (red spectrum). Middle panel: examples of soft-state observations where no significant wind features are found. For epoch #19 the blue edge might be compatible with a P-Cyg feature (see the text). Bottom panel: P-Cyg profiles are absent in the last soft-state observation (#32) but they re-appear over the soft-to-hard transition (epoch #33) with $V_t \sim 2000$ km s^{-1} (dotted line). Yellow shading indicates regions contaminated by interstellar absorption.

We focused the analysis on three narrow spectral ranges covering the following lines: (i) Hα (6563 Å) and the adjacent He I 6678 Å, (ii) He I–5876, and (iii) a third region covering the Bowen blend (mainly N III at 4641 Å) and He II 4686 Å (B+He II hereafter). We have searched for winds in the former two regions, while the last one was used as a proxy for the ionization state of the disk. The three bands are covered by the

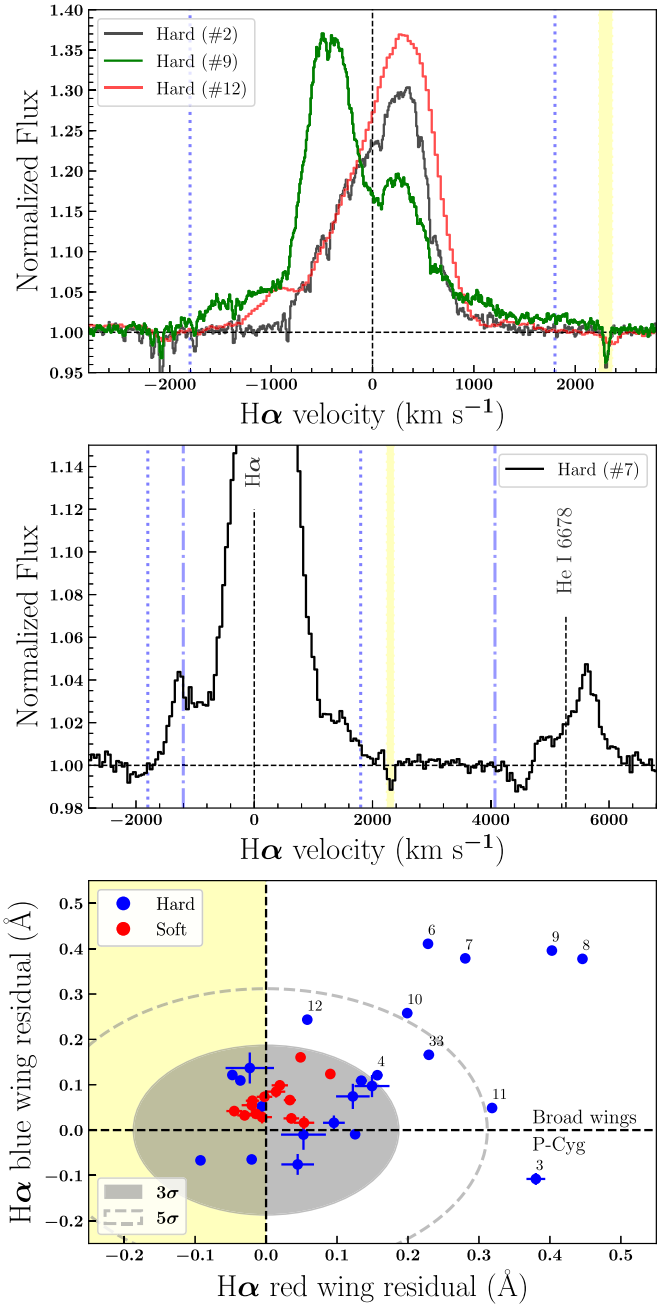

Figure 2. Evolution of Hα. The top panel shows the best examples for asymmetric lines (black, red) and broad emission line wings (green). The middle panel displays epoch #7, where P-Cyg profiles (He I-6678) and broad wings (Hα) are detected. Hα also shows an absorption trough with a blue edge velocity of ~ -1200 km s^{-1}. The two V_t inferred from P-Cyg profiles (He I-5876) at different stages of the outburst (dotted and dashed–dotted lines at ± 1800 and -1200 km s^{-1}) align very closely with the velocities of the Hα wind features. The dashed–dotted line on the right corresponds to -1200 km s^{-1} with respect to He I-6678. Yellow shading indicates regions contaminated by interstellar absorption. Bottom panel: Hα wings diagram. Epochs (note associated numbers) beyond the 5σ contour (dashed line) show conspicuous emission line wings. None of the soft-state data points (red dots) is located beyond the 3σ gray-shadowed area. The left regions of the diagram are forbidden for typical wind features (yellow shading).

whole data set with the exception of He I–5876, which is absent in the (four) Keck and TNG epochs. Every spectral region was carefully normalized in each of the 37 average spectra by fitting the adjacent continuum with a first-order polynomial. This resulted in accurate continuum normalizations that were individually inspected.

In addition, we used data from MAXI to infer the X-ray state at the time of each epoch (see Table 1). We built the hardness-intensity diagram (Homan et al. 2001) using MAXI standard bands and daily averaged fluxes (Figure 3). As was shown by Shidatsu et al. (2019), the system displayed the q-shaped diagram typically observed in BH transients (e.g., McClintock & Remillard 2006; Belloni et al. 2011 for reviews). Our spectroscopic observations cover in great detail the evolution of the system throughout both the hard and soft X-ray states. We define hard and soft spectroscopic epochs as those with X-ray colors[15] higher and lower than 0.4, respectively. As a proxy for the luminosity (i.e., intensity) we used the 2–20 keV MAXI count-rate, but note that a significant amount of the total flux is expected to be below 2 keV during the soft state.

3.1. P-Cygni Profiles

The detection of a P-Cyg profile, first observed in Wolf–Rayet stars (Beals 1929), is conclusive evidence for the presence of an outflow. In compact binaries, however, strong emission line components are naturally produced in their accretion disks (Smak 1969), leaving the blueshifted absorption of the P-Cyg profile as the only unaltered and unambiguous wind signature. Therefore, we have searched for blueshifted absorptions in all our 37 epochs. We initially focused on He I–5876 and subsequently extended the search to the Hα region (see Table 1 for a summary).

Six epochs exhibit broad He I–5876 blueshifted absorptions reaching flux values below 99% of the continuum level (i.e., depth >1%; top panel in Figure 1). Given the quality of our data, we estimate that this is a secure threshold to infer the presence of P-Cyg absorption. Hα also shows wind-related features in five of the six epochs (see below). We will refer to the velocity of the blue edge of the P-Cyg absorption component as the wind terminal velocity (V_t). Following MD16, we estimate V_t by fitting a two-Gaussian model to the data (one in absorption and one in emission) with V_t corresponding to the velocity at 0.1 of the maximum depth of the (fitted) absorption. We find that, although the absorptions are not typically fully Gaussian, this method provides a good description of the depth of the profile and the velocity of the blue edge. During the outburst rise, we measure $V_t = 1206 \pm 13$ km s^{-1} when fitting simultaneously the three GTC observations (#3, #7 and #11), while the individual fits (that includes #2, taken with the VLT) provide consistent (but less constraining) results. Therefore, we take $V_t \sim 1200$ km s^{-1} as the wind velocity during this stage (dashed–dotted, vertical lines in Figure 1). We note that blueshifted absorptions with the same V_t are sometimes detected in Hα and the weaker He I 6678 Å (middle panel in Figure 2). Likewise, we measure $V_t = 1820 \pm 60$ km s^{-1} by fitting observations #33 and #34, and take $V_t \sim 1800$ km s^{-1} as the wind velocity during the outburst decay (dotted vertical lines in Figures 1 and 2). This velocity is significantly larger than that inferred from P-Cyg absorptions during the outburst rise.

Unfortunately, we do not have He I–5876 coverage during epoch #1. However, Hα is very asymmetric toward the red (not shown) and by comparing it with epoch #2 (Figure 2, top panel) taken only 17 hr apart, we notice that the latter is just an evolution

[15] Count-rate ratio between 4–10 keV and 2–4 keV.

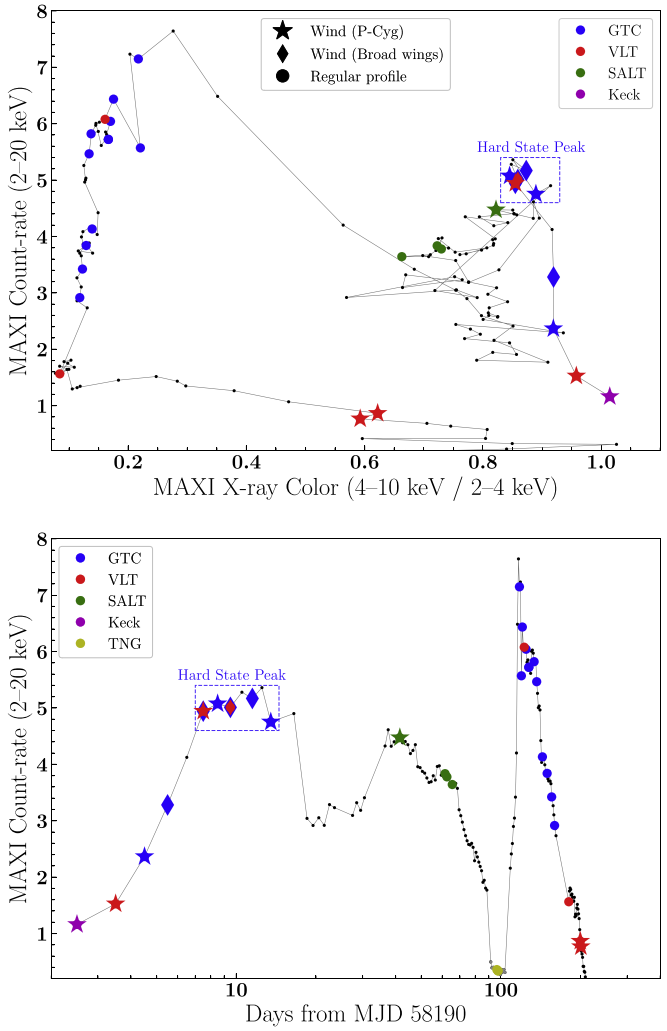

Figure 3. Wind detections as a function of the X-ray outburst evolution. Top panel: hardness-intensity diagram from the MAXI (black dots; daily average light curve). Simultaneous (within 0.5 day) optical observations are marked according to wind signatures and telescope (see the legend). Bottom panel: corresponding MAXI X-ray light curve. Gray points at very low flux (day ∼100) are corrupted and only included to indicate the TNG epoch times. The hard-state peak, when the most conspicuous wind signatures are witnessed, is indicated by blue rectangles.

(toward more asymmetry) of the former. On the other hand, epoch #12 shows a shallow absorption in He I–5876 (∼1%), while Hα is asymmetric, has broad emission line wings and an absorption trough compatible with $V_t \sim 1000$–$1200\,\mathrm{km\,s^{-1}}$ (Figure 2, top panel). Including these two epochs (#1 and #12), we conclude that eight epochs showed P-Cyg features.

Finally, three consecutive epochs (#4, #5 and #6) show a broad emission line wing in He I–5876 (red solid line Figure 1 top panel) reaching $\sim 1200\,\mathrm{km\,s^{-1}}$, hence very similar to V_t measured from P-Cyg absorptions before and after these epochs. This behavior has been also witnessed in V404 Cyg (Mata Sánchez et al. 2018) and we interpret these features as wind detections. The remaining epochs, including every soft-state observation (Figure 1, middle panel), do not show wind signatures in He I–5876 (nor in Hα; see below). A possible exception might be #19, the first soft-state observation, which shows relatively complex and weak blueshifted absorptions (middle panel in Figure 1). Also, we do not detect P-Cyg absorptions during the last three epochs, when the system decayed through the faint hard state below the MAXI detection limit.

3.2. The Hα Spectral Region

Several epochs show broad Hα wings, as well as strong line asymmetries (top panel in Figure 2). Interestingly, the wings extend up to velocities that are remarkably consistent with those derived from the P-Cyg profiles observed months later, during the decay of the outburst (i.e., $V_t \sim 1800\,\mathrm{km\,s^{-1}}$; dotted, vertical lines in Figures 1 and 2). Hence, they exceed $V_t \sim 1200\,\mathrm{km\,s^{-1}}$ measured from He I–5876 in the very same observations. This behavior is clearly exemplified by epoch #7 (hard-state peak). It shows, in addition to a P-Cyg profile in He I–5876 ($V_t \sim 1200\,\mathrm{km\,s^{-1}}$; Figure 1), strong emission line wings in Hα (reaching $\sim 1800\,\mathrm{km\,s^{-1}}$) and a superimposed absorption trough with a blue edge velocity of $-1200\,\mathrm{km\,s^{-1}}$. A (regular) P-Cyg profile in He I 6678 Å at $V_t \sim 1200\,\mathrm{km\,s^{-1}}$ is also present (middle panel in Figure 2).

The strength of Hα and our data's high signal-to-noise allow for a systematic search of wind features using the diagnostic diagram developed in Mata Sánchez et al. (2018) for V404 Cyg. To this end, we performed a Gaussian fit to the line profile that was subsequently subtracted from the data. We masked the innermost part of the line (-300 to $300\,\mathrm{km\,s^{-1}}$ in velocity scale), which can be affected by the double-peak and other line core asymmetries, as well as the emission line wings that we are trying to detect (± 1000 to $\pm 2000\,\mathrm{km\,s^{-1}}$). In the bottom panel of Figure 2 we plot the equivalent width (EW) of residuals in the blue (-1800 to $-1000\,\mathrm{km\,s^{-1}}$) and red (1000 to $1800\,\mathrm{km\,s^{-1}}$) emission line wings.[16] Significance levels are computed by measuring the *EW of the continuum* within masks of the same width (i.e., $800\,\mathrm{km\,s^{-1}}$) in nearby continuum regions. These *continuum residuals* show a Gaussian-like distribution (with mean equal to ∼0) when considering the full sample of spectra. This is used to trace significance contours in Figure 2. The nine epochs with residuals exceeding the 3σ level are hereafter quoted as wind detections (Table 1). They all correspond to hard-state epochs. We note that both the Gaussian fits and the associated residuals were individually inspected, with the most conspicuous cases of broad wings always sitting beyond the 5σ contour. One epoch (#3) sits on the P-Cyg area of the diagram owing to an excess of redshifted emission and lack of blueshifted flux. We consider this an Hα wind detection, although it does not show the standard P-Cyg shape detected in He I–5876 (Figure 1).

4. Discussion

We have presented an optical spectroscopic campaign that is one of the most intensive and sensitive ever carried out on a BH transient in outburst. We have detected wind signatures in the form of P-Cyg profiles and broad emission line wings in several observing epochs during the hard states of the outburst of J1820+070. Such features have been observed before in the BH transients V404 Cyg and V4641 Sgr, although they undergo non-standard outbursts, when only the X-ray hard state, accompanied by strong radio flaring and high X-ray absorption is observed. J1820+070, on the other hand, displayed a standard outburst, showing both hard and soft states across the 8 months spanned by our observations

[16] The masks were shifted by $\pm 200\,\mathrm{km\,s^{-1}}$ for the last five epochs to account for the increasing breadth of the line during the decay.

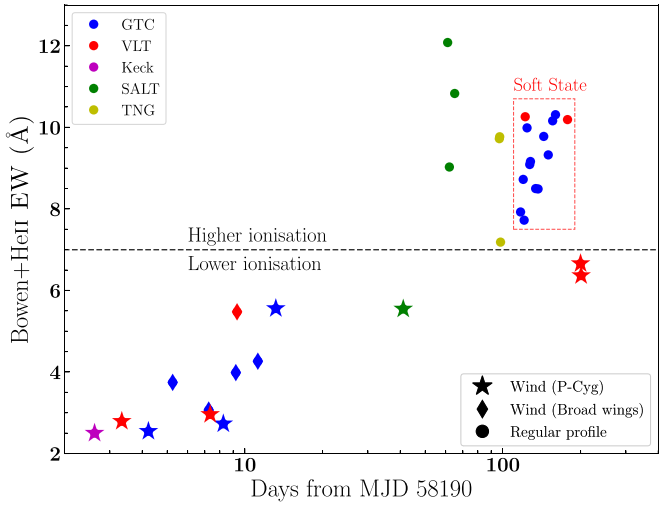

Figure 4. Evolution of B+He II EW with time. Symbols and colors are as in Figure 3 (see the legend). The horizontal dashed line indicates an empirical threshold in EW above which wind signatures are not detected.

(Shidatsu et al. 2019; Figure 3). It is important to note that the wind signatures seen in J1820+070 are significantly shallower than observed in the other two systems (e.g., 1%–2% below the continuum level versus ∼20%). Their detection has only been possible thanks to the combination of the exceptional brightness of the source and our systematic monitoring at very high signal-to-noise. Therefore, these could have been easily missed in other systems, suggesting that cold winds could be a common feature of BH accretion in X-ray binaries.

X-ray winds are typically observed during soft states, but are rarely ever present during BH hard states. Hence, these are mostly detected when the radio jet is quenched (Neilsen & Lee 2009; Ponti et al. 2012), albeit there are some counter-examples (e.g., King et al. 2015; see also Ponti et al. 2014; Díaz Trigo & Boirin 2016; Homan et al. 2016 for neutron star X-ray winds). Figure 3 reveals that the optical wind is almost ubiquitously detected during the hard state, extensively during outburst rise, but also during the decay toward the end of the soft-to-hard transition (Figure 1). In Figure 4 we represent the evolution of the EW of the B+He II emission lines, which—given their higher ionization potential—can be used as a tracer for the state of the disk. All wind detections are found below EW ∼7 Å. This empirical threshold, which is not meant to be accurate and it is also sensitive to variations in the underlying continuum, excludes the whole soft state and some (typically the softest) hard-state epochs (Figure 3). A possible exception to this could be the first soft-state epoch, where a shallow blueshifted absorption might be present in He I–5876 (#19; Figure 1). The B+He II EW from this epoch is just above the ∼7 Å threshold. Therefore, Figure 4 suggests that the non-detection of optical wind features during the soft state might be related to an over-ionization of the ejecta. This was shown to be a key factor for the detectability of the outflow in V404 Cyg (MD16). In addition, some of our most conspicuous wind detections occur at the hard-state peak (epochs #5 to #11; blue rectangle in Figure 3), a stage when radio emission is present (J. Bright et al. 2019, in preparation) and strong jet activity is typically witnessed in BH transients (e.g., Fender et al. 2004). This is also the peak of the optical outburst ($g \sim 11.2$; about 0.8 mag brighter than the soft-state peak), a fact that has been interpreted as being the result of significant jet contribution to the optical regime (Shidatsu et al. 2018, 2019). Therefore, it is clear that the optical wind of J1820+070 is simultaneous with the jet.

We have measured two characteristic wind velocities: $V_t \sim 1200$ and $\sim 1800\,\mathrm{km\,s^{-1}}$. Sometimes these are simultaneously observed in several features of the same spectrum (#7), but also in observations taken months apart. This suggests a rather complex wind structure, and a very appealing scenario would be that they represent different wind-launching mechanisms. However, more detailed modeling, beyond the scope of this discovery work, is needed to support such a scenario (see Muñoz-Darias et al. 2018 for a discussion on optical wind-launching mechanisms). In any case, the obtained V_t are similar to outflow velocities derived from (hard-state) optical winds and (soft-state) X-ray winds in other systems (e.g., MD16, Ponti et al. 2016). This raises the question of whether or not hot and cold winds are intrinsically different or just different observables of the same outflow at different stages of the outburst. In this regard, photoionization instability curves computed by Bianchi et al. (2017) show that the highly ionized soft-state wind might become either fully ionized (hot and low density) or almost neutral (cold and dense) once the system moves to the hard state (and the irradiating spectrum changes accordingly). We are not aware of any X-ray wind detection in J1820+070,[17] but we note that inclination effects play a key role in the detectability of hot outflows (Ponti et al. 2012). Nevertheless, the detection of X-ray dips during the hard state (Homan et al. 2018; Kajava et al. 2019) and the shape of the hardness-intensity diagram (e.g., pronounced hard-state peak; Muñoz-Darias et al. 2013) advocates for a relatively high inclination, which would favor the detection of X-ray outflows.

Finally, it is worth mentioning that the shallowness of the P-Cyg features that we have discovered in J1820+070 might be indicative of a lower-mass outflow rate (e.g., Castor & Lamers 1979) than for the cases of V404 Cyg and V4641 Sgr, where winds have been proposed to significantly affect the outburst evolution (e.g., MD16). In particular, an outflow mass of ∼100 times the accreted mass has been estimated for V404 Cyg (Casares et al. 2019). This could explain the standard outburst displayed by J1820+070 as compared to these objects. Nevertheless, we note that mass outflow rates up to ∼10 times the accretion rate have been proposed for systems displaying regular outbursts and X-ray winds (e.g., Ponti et al. 2012).

5. Conclusions

We have detected optical accretion disk winds during the hard states of the outburst in MAXI J1820+070. Wind signatures are not detected in the soft state, but the visibility of the wind during this stage might be affected by a higher ionization of the accretion disk/ejecta. The detection of the wind has only been possible thanks to the brightness of the source and our exceptionally intensive and sensitive monitoring, implying that similar outflows are likely present in (at least) a significant fraction of BH X-ray binaries. Therefore, wind-like outflows would not be exclusive of bright, hot states but a common mass and angular momentum loss mechanism that operates through most of the accretion episode.

[17] Preliminary analysis of NICER data does not show evidence for soft-state X-ray winds (J. Homan 2019, private communication).

We acknowledge support by the Spanish MINECO under grant AYA2017-83216-P. T.M.D. and M.A.P.T. acknowledge support via Ramón y Cajal Fellowships RYC-2015-18148 and RYC-2015-17854. T.M.D. is thankful to Alex Fullerton for useful discussion on winds from massive stars. D.M.S. acknowledges support from the ERC under the European Unions Horizon 2020 research and innovation programme (grant agreement No. 715051; Spiders). P.A.C. is grateful to the Leverhulme Trust for the award of an Emeritus Fellowship. J.J.E.K. acknowledges support from the Academy of Finland grant 295114. Some of these observations were obtained with the Southern African Large Telescope under the Large Science Programme on transients, 2016-2-LSP-001 (PI: D.A.H.B.). Polish support of this SALT programme is funded by grant No. MNiSW DIR/WK/2016/07. D.A.H.B., E.J.K., and J.T. acknowledge research support from the South African National Research Foundation. D.S. acknowledges support from STFC via grant ST/P000495/1. MOLLY software developed by Tom Marsh is gratefully acknowledged. Based on observations collected at ESO under programmes 0100.D-0292(A) and 0101.D-0158(A).

ORCID iDs

T. Muñoz-Darias https://orcid.org/0000-0002-3348-4035
F. Jiménez-Ibarra https://orcid.org/0000-0002-4634-1076
J. Casares https://orcid.org/0000-0001-5031-0128
G. Ponti https://orcid.org/0000-0003-0293-3608
P. Garnavich https://orcid.org/0000-0003-4069-2817
M. Armas Padilla https://orcid.org/0000-0002-4344-7334
C. Littlefield https://orcid.org/0000-0001-7746-5795

References

Baglio, M. C., Russell, D. M., & Lewis, F. 2018, ATel, 11418, 1
Beals, C. S. 1929, MNRAS, 90, 202
Belloni, T. M., Motta, S. E., & Muñoz-Darias, T. 2011, BASI, 39, 409
Bianchi, S., Ponti, G., Muñoz-Darias, T., & Petrucci, P.-O. 2017, MNRAS, 472, 2454
Bright, J., Fender, R., & Motta, S. 2018, ATel, 11420, 1
Buckley, D. A. H., Swart, G. P., & Meiring, J. G. 2006, Proc. SPIE, 6267, 62670Z
Burgh, E. B., Nordsieck, K. H., Kobulnicky, H. A., et al. 2003, Proc. SPIE, 4841, 1463
Casares, J., Charles, P. A., Jones, D. H. P., Rutten, R. G. M., & Callanan, P. J. 1991, MNRAS, 250, 712
Casares, J., Muñoz-Darias, T., Mata Sánchez, D., et al. 2019, MNRAS, in press
Castor, J. I., & Lamers, H. J. G. L. M. 1979, ApJS, 39, 481
Cepa, J., Aguiar, M., Escalera, V. G., et al. 2000, Proc. SPIE, 4008, 623
Chakravorty, S., Lee, J. C., & Neilsen, J. 2013, MNRAS, 436, 560
Chaty, S., Charles, P. A., Martí, J., et al. 2003, MNRAS, 343, 169
Corral-Santana, J. M., Casares, J., Muñoz-Darias, T., et al. 2016, A&A, 587, A61
Crawford, S. M., Crause, L., Depagne, É., et al. 2016, Proc. SPIE, 9908, 99082L
Díaz Trigo, M., & Boirin, L. 2016, AN, 337, 368
Fabian, A. C. 2012, ARA&A, 50, 455
Fender, R., & Muñoz-Darias, T. 2016, in Lecture Notes in Physics, Vol. 905, ed. F. Haardt et al. (Berlin: Springer), 65
Fender, R. P., Belloni, T. M., & Gallo, E. 2004, MNRAS, 355, 1105
Gatuzz, E., Díaz Trigo, M., Miller-Jones, J. C. A., & Migliari, S. 2019, MNRAS, 482, 2597
Homan, J., Altamirano, D., Arzoumanian, Z., et al. 2018, ATel, 11576, 1
Homan, J., Neilsen, J., Allen, J. L., et al. 2016, ApJL, 830, L5
Homan, J., Wijnands, R., van der Klis, M., et al. 2001, ApJS, 132, 377
Kafka, S., & Honeycutt, R. K. 2004, AJ, 128, 2420
Kajava, J., Motta, S. E., Sanna, A., et al. 2019, MNRAS, in press (arXiv:1906.06519)
Kawamuro, T., Negoro, H., Yoneyama, T., et al. 2018, ATel, 11399, 1
Kennea, J. A., Marshall, F. E., Page, K. L., et al. 2018, ATel, 11403, 1
King, A. L., Miller, J. M., Raymond, J., Reynolds, M. T., & Morningstar, W. 2015, ApJL, 813, L37
Lindstrøm, C., Griffin, J., Kiss, L. L., et al. 2005, MNRAS, 363, 882
Mata Sánchez, D., Muñoz-Darias, T., Casares, J., et al. 2018, MNRAS, 481, 2646
Matsuoka, M., Kawasaki, K., Ueno, S., et al. 2009, PASJ, 61, 999
McClintock, J. E., & Remillard, R. A. 2006, in Compact Stellar X-Ray Sources, ed. W. Lewin & M. van der Klis (Cambridge: Cambridge Univ. Press), 157
Miller, J. M., Raymond, J., Fabian, A., et al. 2006, Natur, 441, 953
Muñoz-Darias, T., Casares, J., Mata Sánchez, D., et al. 2016, Natur, 534, 75
Muñoz-Darias, T., Casares, J., Mata Sánchez, D., et al. 2017, MNRAS, 465, L124
Muñoz-Darias, T., Coriat, M., Plant, D. S., et al. 2013, MNRAS, 432, 1330
Muñoz-Darias, T., Torres, M. A. P., & Garcia, M. R. 2018, MNRAS, 479, 3987
Neilsen, J., & Lee, J. C. 2009, Natur, 458, 481
Neilsen, J., Remillard, R. A., & Lee, J. C. 2011, ApJ, 737, 69
Oke, J. B., Cohen, J. G., Carr, M., et al. 1995, PASP, 107, 375
Ponti, G., Bianchi, S., Muñoz-Darias, T., et al. 2016, AN, 337, 512
Ponti, G., Fender, R. P., Begelman, M. C., et al. 2012, MNRAS, 422, L11
Ponti, G., Muñoz-Darias, T., & Fender, R. P. 2014, MNRAS, 444, 1829
Prinja, R. K., & Fullerton, A. W. 1994, ApJ, 426, 345
Rahoui, F., Tomsick, J. A., Gandhi, P., et al. 2017, MNRAS, 465, 4468
Shidatsu, M., Nakahira, S., Murata, K. L., et al. 2019, ApJ, 874, 183
Shidatsu, M., Nakahira, S., Yamada, S., et al. 2018, ApJ, 868, 54
Smak, J. 1969, AcA, 19, 155
Tetarenko, B. E., Lasota, J.-P., Heinke, C. O., Dubus, G., & Sivakoff, G. R. 2018, Natur, 554, 69
Tucker, M. A., Shappee, B. J., Holoien, T. W.-S., et al. 2018, ApJL, 867, L9
Vernet, J., Dekker, H., D'Odorico, S., et al. 2011, A&A, 536, A105